J Mater Sci: Mater Electron (2018) 29:784–793
DOI 10.1007/s10854-017-7973-4

Calcium doped $BiFeO_3$ films: Rietveld analysis and piezoelectric properties

L. F. Goncalves[1] · L. S. R. Rocha[1] · E. Longo[2] · A. Z. Simões[1]

Received: 24 July 2017 / Accepted: 3 October 2017 / Published online: 20 October 2017

Abstract Pure and calcium modified $Ca_xBi_{(1-x)}FeO_3$ (x = 0.0, 0.1, 0.2, 0.30) thin films were fabricated on Pt(111)/Ti/SiO_2/Si substrates by the soft chemical method. The crystal structure and physical properties of polycrystalline Ca^{2+}-doped $BiFeO_3$ samples have been investigated. Structural studies by XRD reveal the co-existence of distorted rhombohedral and tetragonal phases in the highest doped $BiFeO_3$ where enhanced piezoelectric properties are produced by internal strain. XPS results show that the oxidation state of Fe was purely 3+, which is beneficial for producing a piezoelectric film with low leakage current. Piezoelectric properties are improved in the highest Ca-doped sample due to the coexistence in the crystal structure of BFO with a primitive cubic perovskite lattice with four-fold symmetry and a large tetragonal distortion within the crystal domain. This observation introduces piezoelectronics at room temperature by combining electronic conduction with electric and magnetic degrees of freedom which are already present in the multiferroic $BiFeO_3$.

1 Introduction

Ferro-electromagnets are the class of materials exhibiting the coexistence of magnetic and ferroelectric orderings in a certain range of temperature [1]. Therefore, these materials not only can be used in magnetic and ferroelectric devices but also have the potential ability to couple electric and magnetic polarizations which provides an additional degree of freedom in device design and applications. Consequently, ferro-electromagnetism is the subject of intensive investigations because these materials potentially offer a whole range of applications, including the emerging fields of spintronics, data-storage media, and multiple-state memories [2–6]. Ferromagnetic and ferroelectric ordering parameters are widely used to store binary information in magnetoresistive random access memory (MRAMs) devices [7] and ferroelectric random access memory (FeRAMs) devices [8], respectively. Unfortunately, ferroelectric ferromagnets (or ferrimagnets) are very scarce and the search for a material with both large and finite polarization and magnetization at room temperature is still in progress. To reach this goal, the first step is to obtain materials with magneto-electric coupling. Among all known multiferroics, the only compound that satisfies these criteria is bismuth ferrite (BFO). First synthesized in the late 1950s [9], BFO was shown to be a G-type antiferromagnet with a Néel temperature of 630 K by Kiselev et al. [10]. Later, Sosnowska et al. showed that the magnetic order of bulk BFO is not strictly collinear and that a cycloidal modulation with a period of 62 nm is present [11]. The ferroelectric mechanism in BFO is controlled by the stereochemical activity of the Bi^{3+} $6s^2$ lone pair, responsible of a charge transfer process from $6s^2$ to formally empty 6p orbitals [12, 13] while the weak ferromagnetic property can be associated to the residual moment from the canted Fe^{3+} spin structure [14]. The coupling effect between both magnetic and electric behaviours occurs through lattice distortion of BFO [15] and Khomskii has been emphasized the different ways to combine magnetism and ferroelectricity in mutiferroics materials [16]. The low thermal stability of $BiFeO_3$ provides an obstacle to conventional ceramics processing of this material, as the processing window is very narrow. The formation of

✉ A. Z. Simões
alezipo@yahoo.com

[1] School of Engineering, Sao Paulo State University (Unesp), Guaratinguetá, SP, Brazil

[2] Institute of Chemistry, Sao Paulo State University (Unesp), Araraquara, SP, Brazil

impurity phases such as $Bi_{25}FeO_{39}$ and $Bi_2Fe_4O_9$ provides an additional difficulty in the physical characterization of the paraelectric high-temperature phase [17]. Since part of the problem lies in the volatility of bismuth, doping the A site (Bi site) in $BiFeO_3$ is a key strategy, and there have been some studies on the effect of the replacement of Bi^{3+} with different substituents [18–21]. The doping experiments with Ca^{2+} are of particular interest because they can be exploited to control the band-filling in insulating $BiFeO_3$ thin films, thereby triggering an insulator–metal transition with varying composition [22]. Ramesh et al. studied the quasi-nonvolatile and reversible modulation of electric conduction accompanied by the modulation of the ferroelectric state in Ca-doped $BiFeO_3$ films using an electric field as the control parameter. The mechanism of this modulation in Ca-doped $BiFeO_3$ is based on electronic conduction as a consequence of naturally produced oxygen vacancies that act as donor impurities to compensate Ca acceptors and maintain a highly stable Fe^{3+} valence state [23]. For the low Ca doping regime ($x < 0.1$), films with a monoclinic structure undergo a first-order transition to a pseudo-tetragonal phase at higher temperatures with a thermal hysteresis. The extrapolation of the transition temperature results in the well known ferroelectric Curie temperature (T_c) of $BiFeO_3$ at 1100 K. With increased Ca doping, the ferroelectric T_c rapidly decreases, and a T_c of 600 K with a thermal hysteresis of 240 K is recorded. In fact, many elements have been doped in $BiFeO_3$ for several applications, such as Gd and Co, which were used for the production of a photoanode for hydrogen generation through photoelectrochemical splitting of water, with a maximum photoconversion of 2.29% for the $Bi_{0.9}Gd_{0.1}Fe_{0.75}Co_{0.25}O_3$ (BGFCO-25) system, higher than that of BFO which it is 0.76% [24], or Zr for the production of photocatalysts for methyl orange or Cr(VI) degradation, exhibiting a photocatalytic activity more than two times higher than pure BFO, for 2 mol% Zr-doped system [25], or even Pb combined with La, Sm, Dy or Yb doped BFO, which depicted a higher magnetization value for Yb^{3+} samples along with a multiferroic behavior for $Bi_{0.92}Pb_{0.04}RE_{0.04}FeO_3$ (RE = La, Sm, Dy, Yb) crystallites [26]. Other dopants such as La were also used for producing $BiFeO_3$ doped systems by the sol–gel route, depicting an enhanced magnetization due to the substitution with lanthanum ions [27], as well as a very strong coercitivity H_c of 19.5 kOe [28], or even Er-doped BFO thin films prepared by a spin-coating processing showing a surprising remnant polarization nearly five times higher than that of pure $BiFeO_3$. Our group has expanded significant effort in developing synthetic routes of $BiFeO_3$ thin films [29, 30] and we have previously reported the preparation of Ca-doped $BiFeO_3$ thin films grown on Pt(111)/Ti/SiO_2/Si substrates with good fatigue and retention properties, along with a higher ferroelectric polarization of 51 μC/cm^2 for the Ca-doped BFO [31], when compared to 40 μC/cm^2 for a composition of $Bi_{0.875}Sm_{0.125}FeO_3$. In the present investigation and as a natural extension of previous work, structural and electrical properties of the films, mainly related to piezoelectric behavior were investigated by using various techniques with a view to exploring their technological applications. We expected that doping with Ca^{2+} on the A site of $BiFeO_3$ will reduce the number of Bi^{3+} ions which will, in turn, reduce the collective number of stereochemically active $6s^2$ lone pairs affecting the degree of off-centering of the FeO_6 octahedra and thus also the piezoresponse properties of $BiFeO_3$.

2 Experimental procedure

Ca-modified $BiFeO_3$ thin films were prepared by the PPM as described elsewhere [31]. Films were spin coated on Pt/Ti/SiO_2/Si substrates by a commercial spinner operating at 5000 revolutions/min for 30 s (spin coater KW-4B, Chemat Technology). An excess of 5% wt of Bi was added to the solution to minimize bismuth loss during thermal treatment. Thin films were annealed at 500 °C for 2 h in a conventional furnace under static air atmosphere. The film thickness was reached by repeating spin-coating and heating treatment cycles ten times. Annealed film thicknesses were measured using SEM (Topcom SM-300) at the transversal section. We have obtained films with thicknesses in the range of 340–360 nm. A phase analysis of films was performed at room temperature by XRD using a Bragg–Brentano diffractometer (Rigaku 2000) and CuKα radiation; in this case, back scattering electrons were used. The Rietveld analysis was performed with the Rietveld refinement program DBWS-941 1 [32]. The profile function used was the modified Thompson-Cox-Hastings pseudo-Voigt where η (the Lorentzian fraction of the function) varies with the Gauss and Lorentz components of the full width at half maximum. The morphology of the films was observed using a high-resolution FEG-SEM (Supra 35-VP, Carl Zeiss, Germany). Raman measurements were performed using an ISA T 64,000 triple monochromator. An optical microscope with 80 X objective was used to focus the 514.5-nm radiation from a Coherent Innova 99 Ar^+ laser on the sample. The same microscope was used to collect the back-scattered radiation. The scattering light dispersed was detected by a charge-coupled device (CCD) detection system = 0.3 mm. A PHI-5702 multifunction X-ray photoelectron spectrometer (XPS) was used, with an Al-Kα X-ray source of 29.35 eV passing energy. The chamber pressure during the experiments was about 4.5×10^{-9} Torr. The calibration of the binding energy scale was controlled using the C1s line which appears in photoelectron spectra of the as-grown samples. Top Au electrodes (0.5 mm diameter) were prepared for electrical measurements by evaporation through a shadow

mask at room temperature. The leakage current–voltage (I–V) characteristic was determined by a voltage source measuring unit (Radiant Technology 6000 A). Piezoelectric properties were carried out using a setup based on an atomic force microscope in a Multimode Scanning Probe Microscope with Nanoscope IV controller (Veeco FPP-100). In our experiments, piezoresponse images of the films were acquired in ambient air by applying a small ac voltage with an amplitude of 2.5 V (peak to peak) and a frequency of 10 kHz while scanning the film surface. To apply the external voltage we used a standard gold coated Si_3N_4 cantilever with a spring constant of 0.09 N/m. The probing tip, with an apex radius of about 20 nm, was in mechanical contact with the uncoated film surface during the measurements. Cantilever vibration was detected using a conventional lock-in technique.

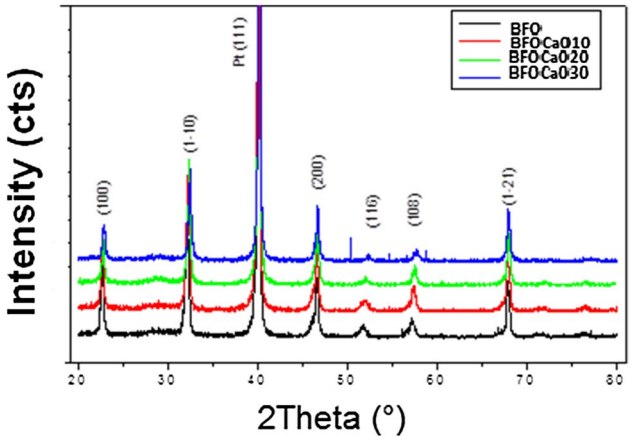

Fig. 1 X-ray diffraction of BFO, BFOCa010, BFOCa020, BFOCa030 thin films deposited by the polymeric precursor method and annealed at 500 °C in static air for 2 h

3 Results and discussion

Figure 1 illustrates the XRD patterns of BFO and Ca-doped BFO films deposited on platinum-coated silicon substrates. The films were well crystallized at a processing temperature of 500 °C. BFO and Ca-doped BFO films self-organized to produce (110)-preferred orientation with good crystallinity. With the partial substitution of Ca ions for A-site bismuth ions, the BCFO film (108) diffraction peak shifted toward

Table 1 Index refinements for BFO, BFOCa010, BFOCa020 and BFOCa030 thin films annealed at 500° for 2 h

Parameter	BFO	BFOCa010	BFOCa020	BFOCa030
Refinement index				
Rwp (%)	8.14	5.97	5.51	4.59
Rexp	4.67	3.91	3.76	3.31
S	1.74	1.52	1.46	1.38
Atomic positions				
A1	0; 0; 0.06722	0; 0; 0.06712	0; 0; 0.06720	0; 0; 0.06733
A2	0; 0; 0.21091	0; 0; 0.21023	0; 0; 0.21132	0; 0; 0.21145
B1	0; 0; ½	0; 0; ½	0; 0; ½	0; 0; ½
B2	0; 0; 0.37099	0; 0; 0.37213	0; 0; 0.37143	0; 0; 0.37120
O1	¼; ¼; 0	¼; ¼; 0	¼; ¼; 0	¼; ¼; 0
O2	¼; ¼; ¼	¼; ¼; ¼	¼; ¼; ¼	¼; ¼; ¼
O3	0; 0; 0.43786	0; 0; 0.43747	0; 0; 0.43616	0; 0; 0.43638
O4	0; 0; 0.32536	0; 0; 0.31851	0; 0; 0.31895	0; 0; 0.31989
O5	¼; ¼; 0.11165	¼; ¼; 0.11584	¼; ¼; 0.11580	¼; ¼; 0.11581
S_{Occ}				
Bi (A1)	1.00000	0.87500	0.75000	0.62500
Ca(A1)	0.00000	0.12500	0.25000	0.37500
O	0.91700	0.91000	0.91800	0.94900
Lattice parameter				
a (Å)	5.577352	5.576058	5.577687	5.578439
c (Å)	13.867785	13.807185	13.773235	13.764944
V ($Å^3$)	373.529	371.784	371.086	370.963
t	0.915	0.916	0.919	0.920
Perovskite (mol%)	97.5 ± 0.5	97.1 ± 0.4	98.4 ± 0.4	97.7 ± 0.4
Stoichiometry	$BiFeO_3$	$Bi_{0.9}\ Ca_{0.1}FeO_3$	$Bi_{0.80}\ Ca_{0.2}FeO_3$	$Bi_{,0.70}\ Ca_{0.30}FeO_3$
Refinement	$BiFeO_{2.6}$	$Bi_{0.9}\ Ca_{0.1}FeO_{2.6}$	$Bi_{0.80}\ Ca_{0.2}FeO_{2.6}$	$Bi_{0.70}\ Ca_{0.30}FeO_{2.8}$

a higher angle. No additional peak related to CaO could be assigned by revealing partial substitution of Ca by bismuth in the crystal lattice and solid solution of Ca substitution in BFO. The BCF030 film has a tetragonal structure with a *P4mm* space group while BFO has a rhombohedral structure with an *R*3*c* space group which can be treated as a special triclinic structure. To verify and confirm the structure of BCFO thin films a structural refinement by the Rietveld method was performed. The Rietveld method is a least squares refinement procedure where the experimental step-scanned values are adapted to calculated values. The profiles are considered to be known, and a model for a crystal structure is available [33]. This structural refinement method presents several advantages over conventional quantitative analysis methods because this method uses a whole pattern fitting algorithm where all lines for each phase are explicitly considered, and even severely overlapped lines are usually not a problem. Thus, it is not necessary to decompose patterns into separate Bragg peaks as is often the case for traditional methods. The use of all reflections in a pattern rather than just the strongest reflections minimizes both uncertainty in derived weight fractions and effects of preferred orientation, primary extinction and nonlinear detection systems [34]. The structural refinement was performed by using a Maud program [35] which employs the Rietveld texture and stress analysis [36]. According to the literature [37], the quality of data from structural refinement is generally checked by R-values (R_{wp}, R_{exp}, and S). The quality of structural refinement also can be verified by the R_{wp} factor value. Its absolute value does not depend on the absolute value of the intensities; instead, it depends on the background with a high background, it is easier to reach very low values. Increasing the number of peaks (sharp peaks) created more difficulty in obtaining a good value. Structural refinement data are acceptable when the R_{wp} is $< 10\%$ for a medium complex phase, when high complex phases (monoclinic to triclinic), have a value of $R_{wp} < 15\%$ and when a highly symmetric material or compound (cubic) with few peaks has a value of $R_{wp} < 8\%$ [33, 38]. Table I lists R_{wp}, $R_{exp,}$ and S indexes as well as lattice parameters (*a* and *c*) and the unit cell volume (V). Atomic positions obtained by Rietveld analyses belong to the ICSD card (86-1518). Quantitative phase analyses of powders for the rhombohedral phase were calculated according to Young and Wiles [32]. Results obtained confirm that the Bi^{3+} ion was substituted by the Ca^{2+} ion in the rhombohedral BFO phase, and no changes occurred in refinements. Ca^{2+} substitutes for Bi^{3+} only in a perovskite-type unit cell which causes a distorted structure whereby distortion increases with a higher Ca content, as shown in Fig. 2. The covalent interaction which originates from the strong hybridization between Fe 3*d* and O 2*p* orbitals plays an important role in the structural distortion of the BFO lattice. Doping with Ca improves oxygen ion stability in the lattice because some of the Bi ions in the pseudo-perovskite layers containing Fe–O octahedra are substituted by the rare earth ion. From low S values ($S = R_{WP}/R_{exp}$), it can be assumed that the refinement was successfully performed with all the investigated parameters close to literature data [39]. It can be inferred that the *c*-axis is less elongated after Ca addition which is caused by differences in charge densities of Ca and bismuth atoms. Also, the addition of Ca has a radial substitution effect higher than bismuth and stabilizes oxygen vacancies and consequently the structure. The decrease in the lattice parameter and unit cell volume is almost linear as expected due to the stoichiometric replacement of Bi^{3+} with a smaller ionic radii substituent (in this case Ca^{2+}). The results obtained from the structural refinement are displayed in Table 1. In this table, the fitting parameters (R_{wp}, R_{exp}, and

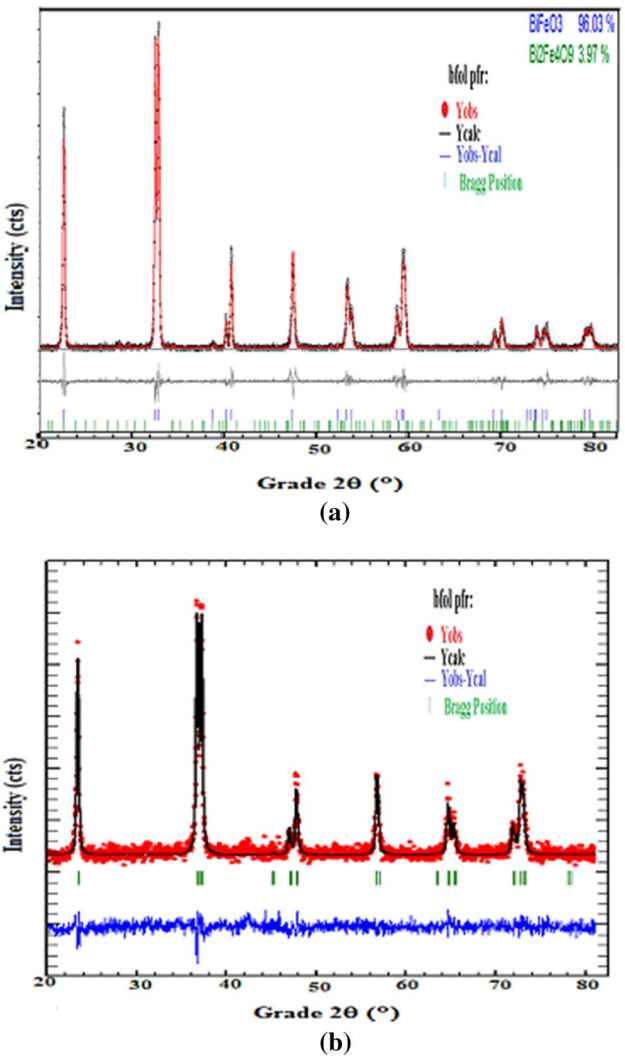

Fig. 2 Rietveld plots of **a** BFO and **b** BFOCa030 thin films deposited by the polymeric precursor method and annealed at 500 °C in static air for 2 h

S) indicate good agreement between refined and observed XRD patterns. Small variations in lattice parameters, unit cell volumes and displacements on Fe atoms (network formers) are indicative of distortions/strain in the lattice caused by differences in crystal lattice parameters and the thermal expansion behaviour between the film and the underlying substrate or arising from defects promoted by [BiO_{12}] and [CaO_{12}] clusters (network modifiers).

Raman analysis shows the order–disorder degree of the atomic structure at short range (see Fig. 3). The modes further split into longitudinal and transverse components due to long electrostatic forces associated with lattice ionicity. The substitution of calcium at the A-site lattice reduces the distortion of octahedral clusters having little influence on the relative intensity of the bands. The vibrational modes located at 226, 357, 385, 529, and 562 cm^{-1} result from the FeO_6 octahedron (Fe = 5 or Fe = 6). The band located below 200 cm^{-1} is due to the site occupied by bismuth within the perovskite layer. Slight changes which occur above 200 cm^{-1} in the doped films can be associated with structural distortion and the reduction of vibrations in the FeO_5 octahedra. Calcium substitution has a marginal influence in the interactions between the $(Bi_2O_2)^{2+}$ layers and perovskite structure. The vibrational modes of the BCF030 thin film tend to disappear when compared to the BFO thin film. Structural rearrangements take place during the energy transfer process creating distortion across the octahedral (FeO_6) and dodecahedral (BiO_{12}) clusters. In this way, there is a symmetry breaking process along the network of both [FeO_6] and [BiO_{12}] clusters leading to lower symmetry. This can be related to structural disordering at short range, as well as a phase transition for an ordering crystal structure. Thus, it appears that doping $BiFeO_3$ with Ca^{2+} affects the perovskite-related phonon modes which are associated with a tilting of the FeO_6 octahedra, the motion of oxygen atoms associated with the Bi site and

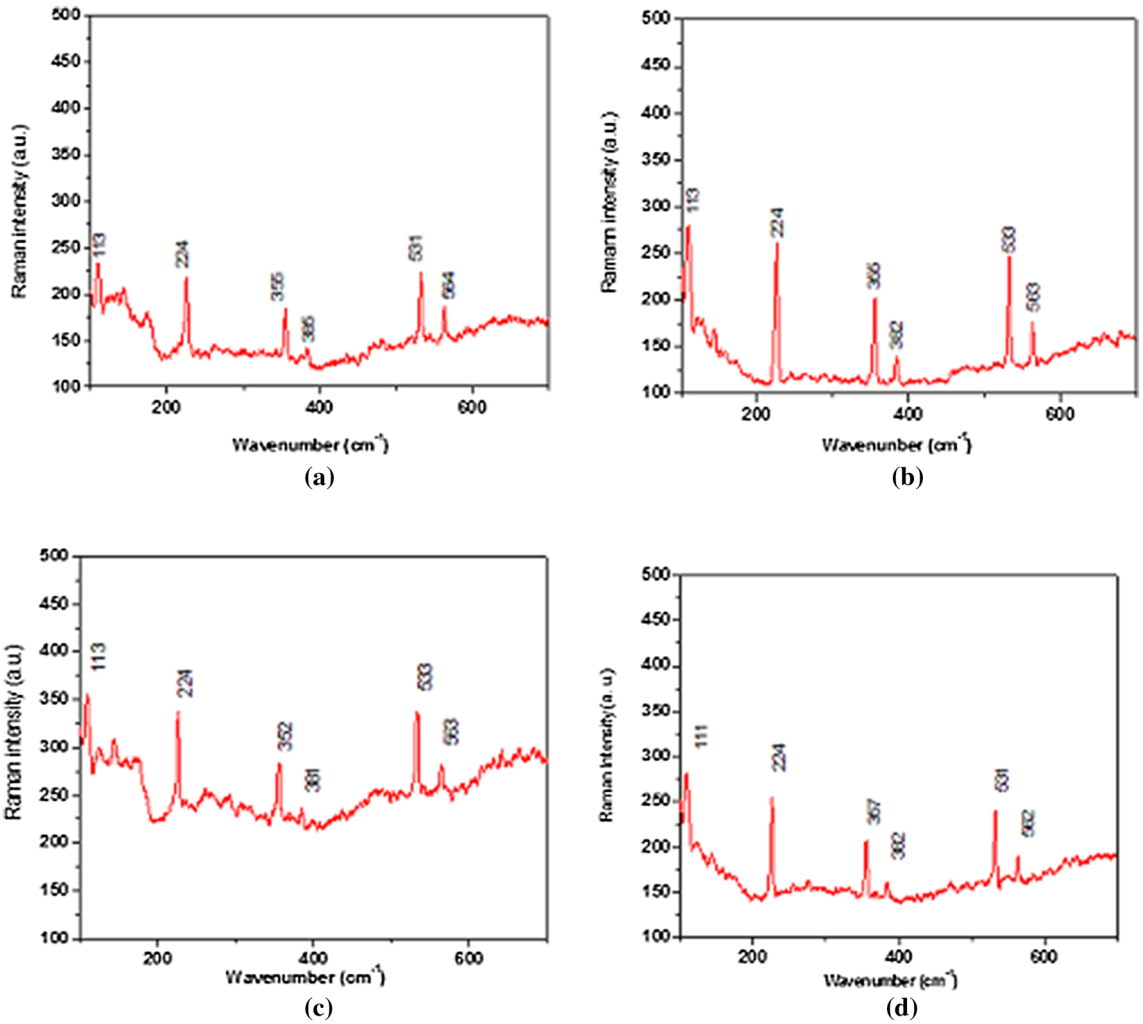

Fig. 3 Micro-Raman of thin films deposited by the polymeric precursor method and annealed at 500 °C in static air for 2 h. **a** BFO, **b** BFOCa010, **c** BFOCa020 and **d** BFOCa030

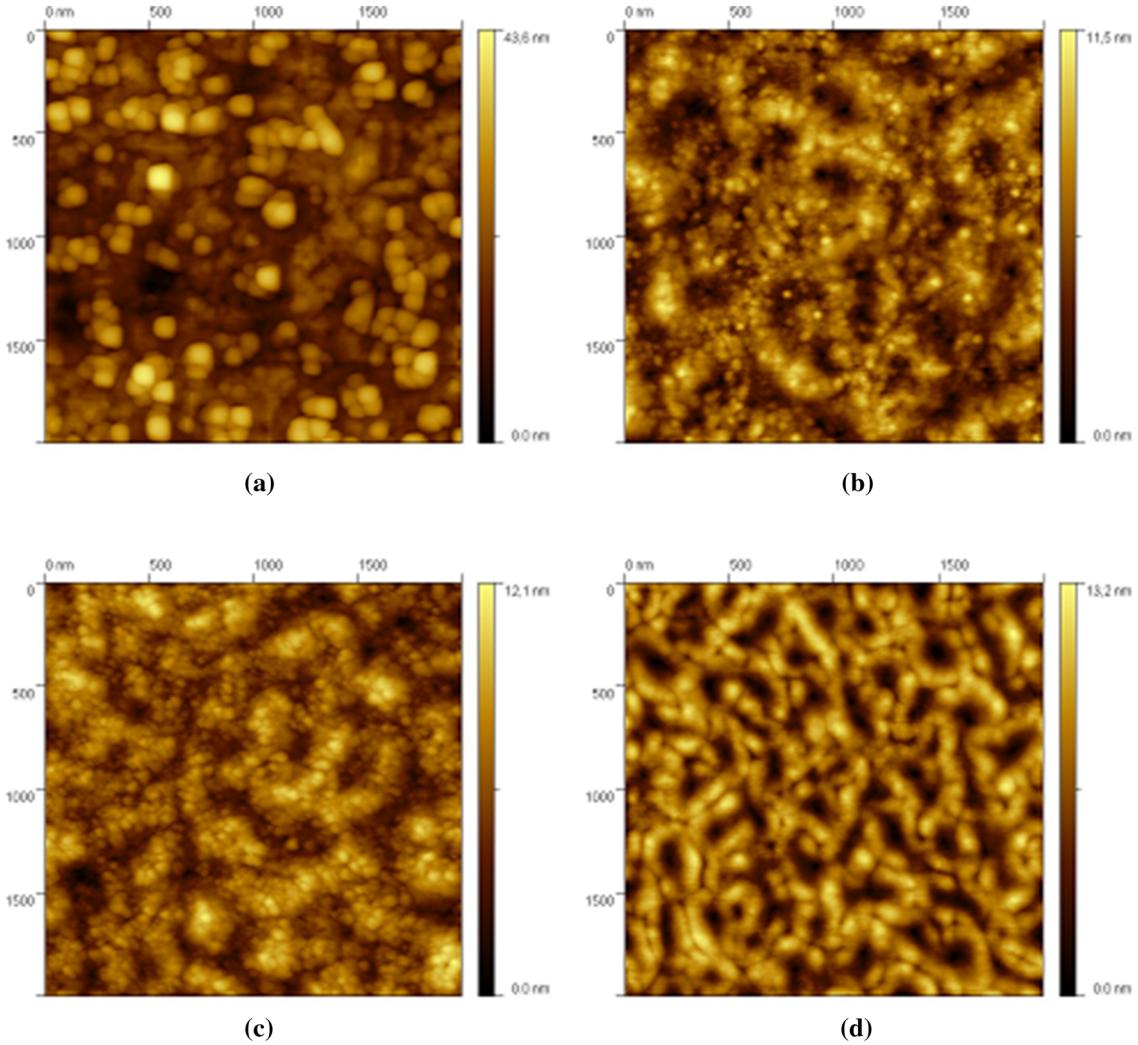

Fig. 4 AFM micrographies of thin films deposited by the polymeric precursor method and annealed at 500 °C in static air for 2 h. **a** BFO, **b** BFOCa010, **c** BFOCa020 and **d** BFOCa030

the off-centering of the Fe from its special crystallographic position.

The surface morphology of the BFO and Ca-doped BFO thin films was evaluated by AFM measurements (Fig. 4). AFM studies demonstrated that Ca as a dopant reveals a homogeneous surface indicating that the soft chemical method allows the preparation of films with controlled morphology. Changes in the surface of the Ca-doped BFO films were evaluated and the results reveal that the BCF030 film consists of a homogeneous surface although BFO film has a degree of porosity. It was also found that the Ca dopant tends to suppress grain growth. BCF030 was found to be effective in improving the surface morphology of synthesized BFO-based films because the precursor film underwent the optimized nucleation and growth process to produce films with a homogeneous and dense microstructure. On the other hand, for low and middle Ca concentrations, the surface consists of irregularities which were caused by distortion in the lattice caused by Ca addition. The average grain size is 63 nm for the BFO film and 33 nm for the highest doped film. The substitution of Ca^{2+} for Bi^{3+} in $BiFeO_3$ can produce oxygen vacancies which apparently induce distortions and causes structural irregularities within the crystallites. Also, the homogeneous microstructure of BCF030 films may affect the piezoelectric properties because the voltage can be uniformly applied on them. The average surface roughness value is 6.2 nm for the BFO thin film, 6.1 nm for the BCF010 film, 5.8 nm for the BCF020 film and for the BCF030 film consists of a statistical roughness with a root mean square (RMS) of approximately 5.5 nm.

To identify the chemical bonding of thin films, XPS measurements were performed on the deposited surface.

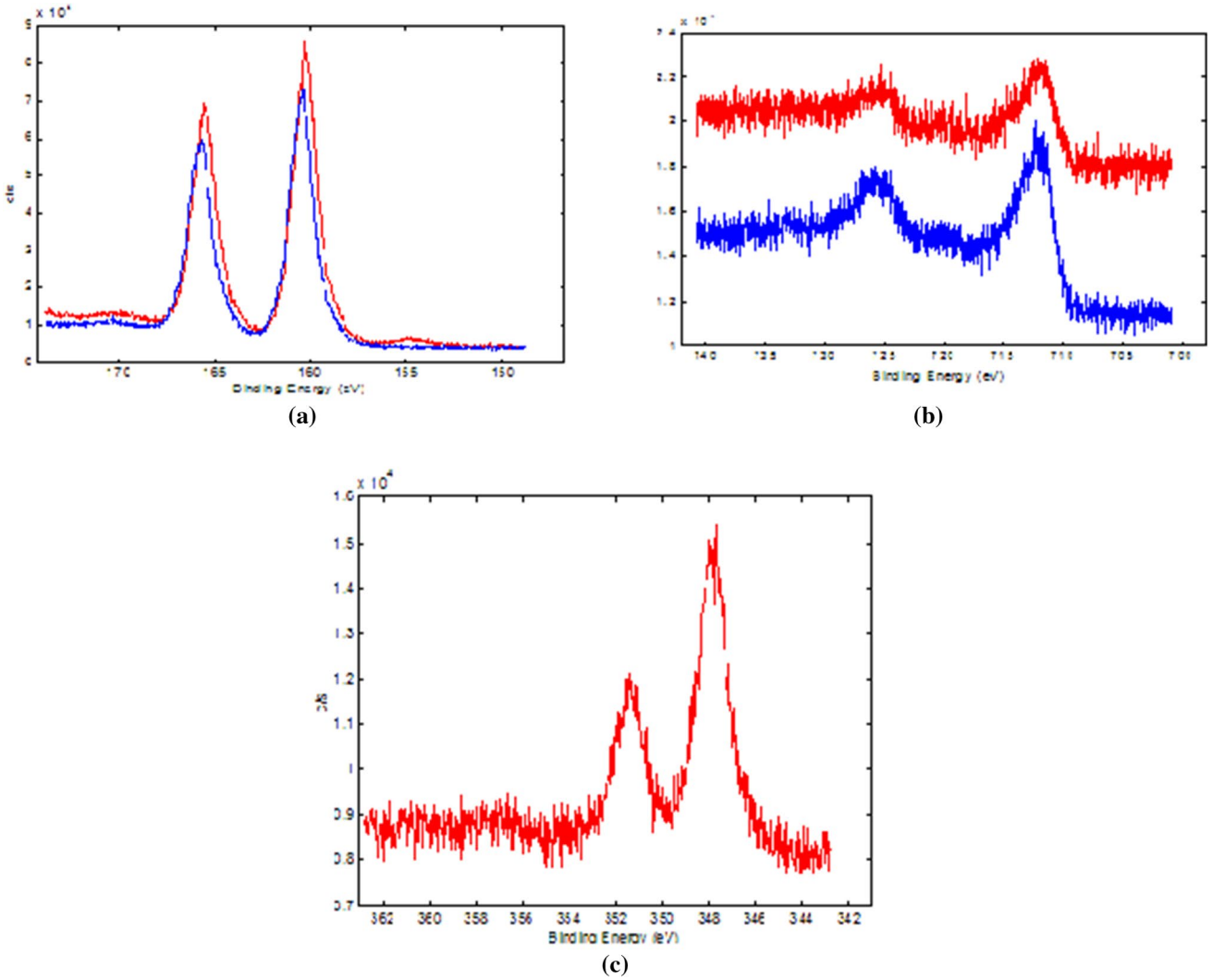

Fig. 5 XPS spectra for BFO (blue) and BFOCa030 (red) thin films deposited by the polymeric precursor method and annealed at 500 °C in static air for 2 h related to **a** Bi 4f, **b** Fe 2p and **c** Ca 2p orbitals

The spectrum expanded from 700 to 745 eV (see Fig. 5). The 3/2 and 1/2 spin–orbit doublet components of the Fe 2*p* photoemission located at 711.1 and 724.6 eV, respectively, were identified as Fe^{3+}; no Fe^{2+} and Fe were found. XPS results show that BCF030 thin films have a single phase with a Fe^{3+} valence state. The oxidation state of Fe was purely 3+, which was advantageous for producing thin films with low leakage current. BFO thin films reveal the same XPS spectra with the 3/2 and 1/2 spin–orbit doublet components of the Fe 2*p* photoemission located at 711.1 and 724.6 eV.

The insulating properties of the films were found to be dependent on the calcium substitution. A typical leakage current characteristic of the films is given in Fig. 6. The curves were recorded with a voltage step width of 0.1 V and elapsed time of 1.0 s for each voltage, here the measured logarithmic current density (log J) versus the logarithmic electric field (E) is shown. It can be seen that there are two clearly different regions. The current density increases linearly with the external electric field in the region of low electric field strengths, suggesting an ohmic conduction. At higher field strengths the current density increases exponentially, which implies that at least one part of the conductivity results from Schottky or Poole–Frenkel emission mechanism. The leakage current density at 1.0 V slight increases for the BCF010 and BCF020 films. As the applied field increased, defects such as oxygen vacancies interacted strongly with domains boundaries and had significant influences on the conducting process. An increase in conductivity with increasing oxygen content indicates that the mobile carriers are positively charged and that the possibility of hopping through the Bi ion can be considered. The measured leakage current density at 1.0 V for the BCF030 film

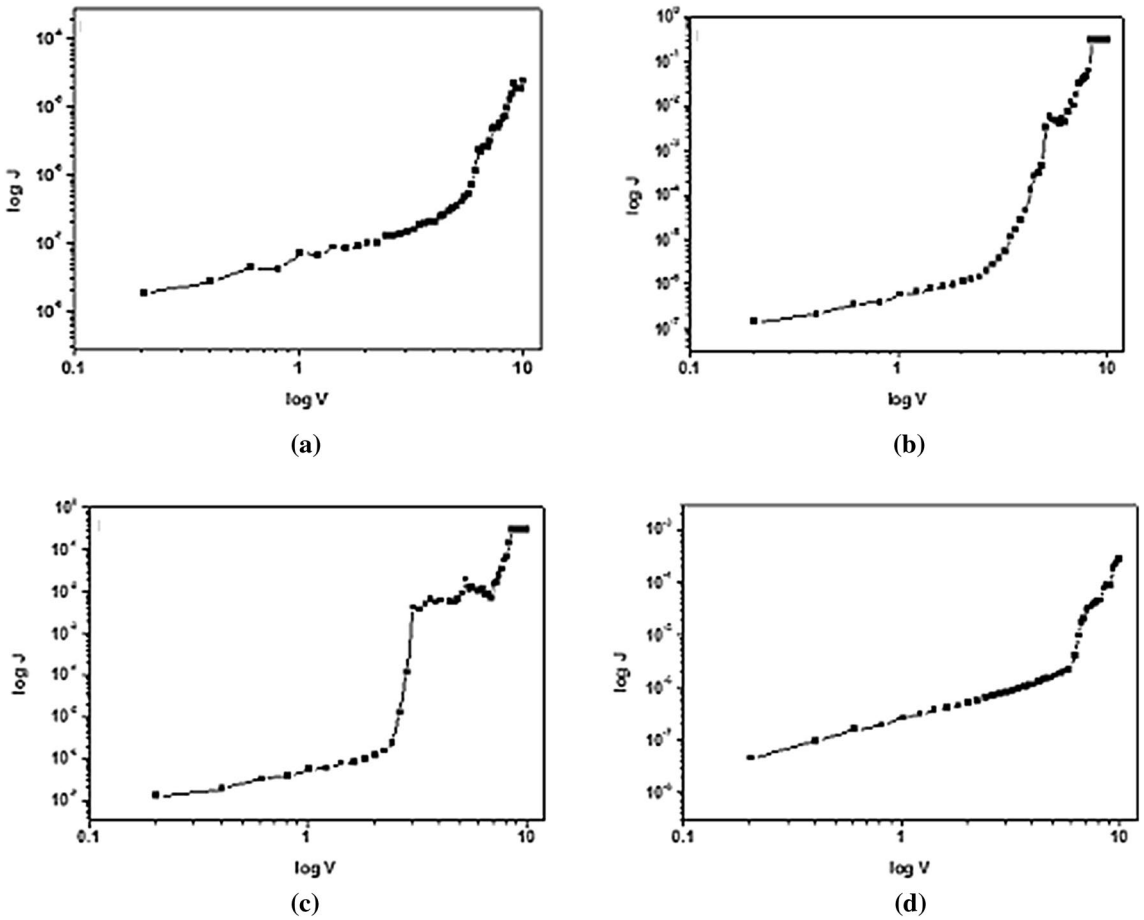

Fig. 6 Typical *I–V* hysteresis curve of thin films deposited by the polymeric precursor method and annealed at 500 °C in static air for 2 h. **a** BFO, **b** BFOCa010, **c** BFOCa020 and **d** BFOCa030

decreases to 10^{-09} A/cm^2 indicating that the main carrier type which produces observed transport behaviour must be electronic rather than ionic in nature. This suggested that the conduction on calcium substituted is mainly governed by thermally activated hopping of electrons between oxygen vacancy related defects which is inconsistent with the vacancy assisted electronic conduction mechanism observed in epitaxial thin films.

The piezoelectric properties are found to be dependent on Ca substitution, as shown in Fig. 7. The BCF010 and BCF020 films possess highly diminished piezoelectricity, which completely improves for the BCF030 film, due to the coexistence of a junction between both rhombohedral and tetragonal crystalline structures, as proposed by Tian [40] and Zhang et al. [41], which demonstrated that the junctions boosts the functions. The hysteresis in the piezoresponse signal is directly associated with the polarization switching and ferroelectric properties of the sample. Although the piezoresponse signal shows no activity for the BCF010 and BCF020 films, a narrow loop is evident. For the BCF030 film, the shape of the loop is similar to a dielectric material indicating that is easier to switch the domains. Here, we point out that it is difficult to compare these values to the piezoelectric coefficients of bulk material since the measurement was performed on a local area that has a relatively intricate field distribution and vibrational modes. Considering the polycrystalline nature of our films the effective piezoelectric coefficient depends on grain orientation and surface characteristics. The BCFO30 film presents a symmetric hysteresis loop which is indicative that calcium stabilizes the charged domain walls which interact with oxygen vacancies and reduce the coercive field. Adding Ca^{2+} ions to BFO in high concentrations requires charge compensation which can be achieved by the formation of Fe^{4+} or oxygen vacancies. If Fe^{4+} exists, the statistical distribution of Fe^{3+} and Fe^{4+} ions in the octahedron may also lead to strong polarization while high coercivity can be caused by the pinning of ferroelectric domain walls which results from the ferroelectric anisotropy.

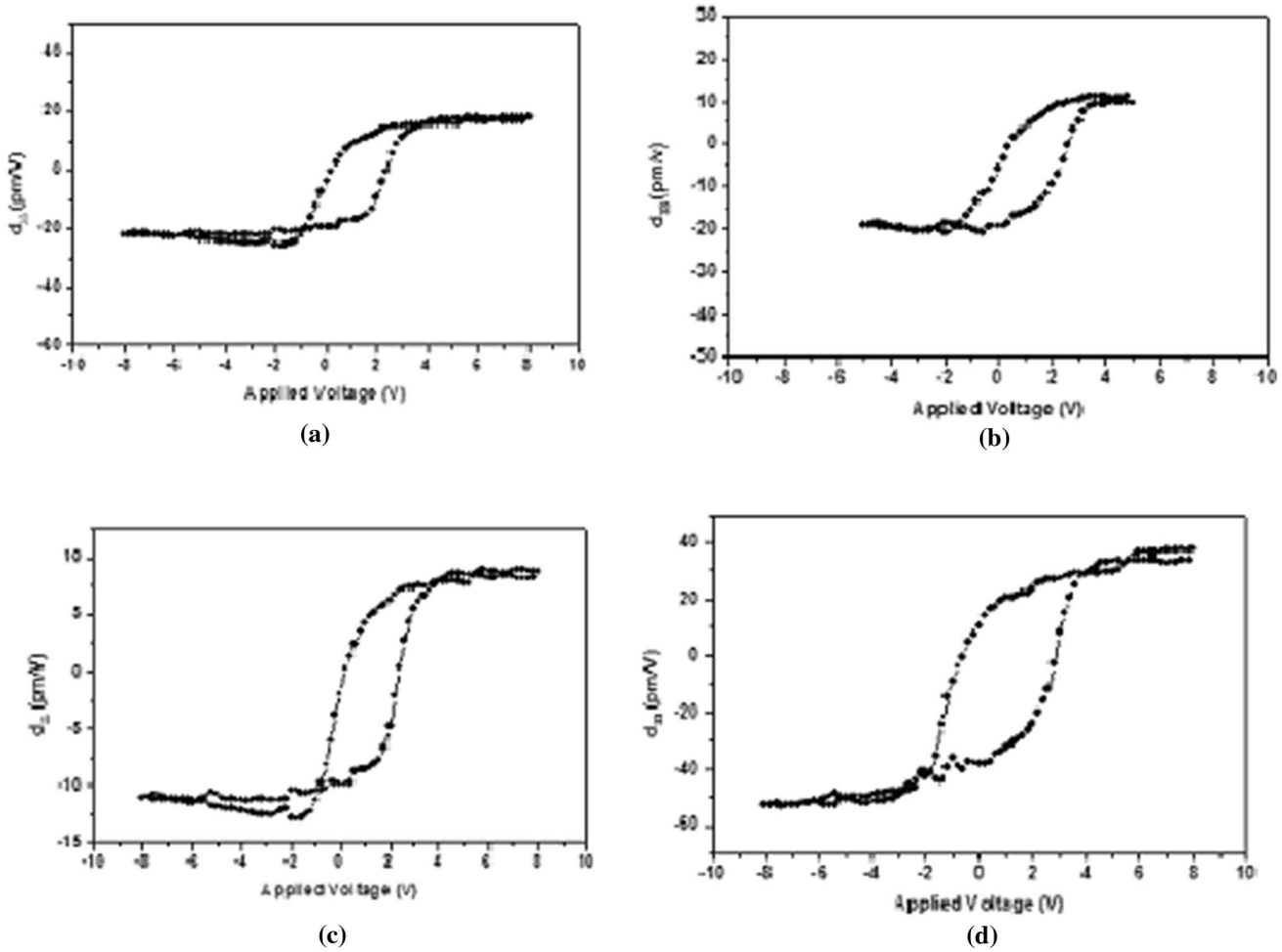

Fig. 7 Piezoresponse loops of thin films deposited by the polymeric precursor method and annealed at 500 °C in static air for 2 h. **a** BFO, **b** BFOCa010, **c** BFOCa020 and **d** BFOCa030

4 Conclusions

In summary, we have demonstrated a viable chemical deposition process which enables the growth of good quality BFO and Ca-based $BiFeO_3$ multiferroic thin films. The highest Ca concentration changes the local distortion and strain caused by the rhombohedral co-existing phase which is reflected in physical properties of the system. Leakage current data reveals that the electrical conduction in these samples occurs via oxygen vacancy hopping. Among these films studied, the BCFO30 film exhibited a better micro-structure with low leakage and as well as better piezoelectric response. The results of these studies are very promising and suggest that BCFO30 thin films are attractive for use as a storage element in nonvolatile ferroelectric and piezoelectric transducers.

Acknowledgements The financial support of this research project by the Brazilian research funding agencies CNPq 573636/2008-7, INCTMN 2008/57872-1 and FAPESP 2013/07296-2.

References

1. E.V. Salje, *Phase transitions in ferroelastic and co-elastic crystals*. (Cambridge University Press, Cambridge, 1990)
2. M. Fiebig, T. Lottermoser, D. Fröhlich, A.V. Golsev, R.V. Pisarev, Observation of coupled magnetic and electric domains. Nature **419**, 818–820 (2002)
3. N.A. Hill, Why are there so few magnetic ferroelectrics? J. Phys. Chem. B **104**, 6694–6709 (2000)
4. G.A. Smolenskii, I.E. Chupis, Ferroelectromagnets. Sov. Phys. Usp. **25**, 475–493 (1982)
5. J. Wang, J.B. Neaton, H. Zheng, V. Nagarajan, K.M. Rabe, M. Wuttig, R. Ramesh, Epitaxial $BiFeO_3$ multiferroic thin film heterostructures. Science **299**, 1719–1722 (2003)
6. J. Li, J. Wang, M. Wuttig, R. Ramesh, B. Wang, B. Ruette, A.P. Pyatakov, A.K. Zvezdin, D. Viehland, Dramatically enhanced polarization in (001), (101) and (111) $BiFeO_3$ thin films due to epitaxial-induced transitions. Appl. Phys. Lett. **84**, 5261–5263 (2004)
7. W.J. Gallagher, S.S.P. Parkin, Development of the magnetic tunnel junction MRAM at IBM: from first junctions to a 16-Mb MRAM demonstrator chip. IBM J. Res. Dev. **50**, 5–23 (2006)

8. D. Dawber, K.M. Rabe, J.F. Scott, Physics of thin-film ferroelectric oxides. Rev. Mod. Phys. **77**, 1083–1130 (2005)
9. P. Royen, K. Swars, Das system Wismutoxyd-Eisenoxyd im Bereich von 0 bis 55Mol% Eisenoxyd. Angew. Chem. **24**, 779–781 (1957)
10. S.V. Kiselev, R.P. Ozerov, G.S. Zhdanov, detection of magnetic order in ferroelectric $BiFeO_3$ by neutron diffraction. Sov. Phys. Dokl. **7**, 742–744 (1963)
11. I. Sosnowksa, T. Peterlin-Neumaier, E. Steichele, Spiral magnetic ordering in bismuth ferrite. J. Phys. C **15**, 4835–4846 (1982)
12. Y. Wang, C.W. Nan, Effect of Tb doping on electric and magnetic behavior of $BiFeO_3$ thin films. J. Appl. Phys. **103**, 024103 (2008)
13. J. Liu, M.Y. Li, L. Pei, B.F. Yu, D.Y. Guo, X.Z. Zhao, Effect of Ce doping on the microstructure and electrical properties of $BiFeO_3$ thin films prepared by chemical solution deposition. J. Phys. D **42**, 115409 (2009)
14. J. Liu, M.Y. Li, L. Pei, J. Wang, B.F. Yu, X. Wang, X.Z. Zhao, Structural and multiferroic properties of the Ce-doped $BiFeO_3$ thin films. J. Alloys Compd. **493**, 544 (2010)
15. A. Lahmar, S. Habouti, M. Dietze, C.H. Solterbeck, M. Es-Souni, Effects of rare earth manganites on structural, ferroelectric, and magnetic properties of $BiFeO_3$ thin films. Appl. Phys. Lett. **94**, 012903 (2009)
16. Y. Wang, C.W. Nan, Structural and ferroic properties of Zr-doped $BiFeO_3$ thin films. Ferroelectrics **357**, 172 (2007)
17. H. Naganuma, J. Miura, S. Okamura, Ferroelectric, electrical and magnetic properties of Cr, Mn, Co, Ni, Cu added polycrystalline $BiFeO_3$ films. Appl. Phys. Lett. **93**, 052901 (2008)
18. P. Kharel, S. Talebi, B. Ramachandran, A. Dixit, V.M. Naik, M.B. Sahana, C. Sudakar, R. Naik, M.S.R. Rao, G. Lawes, Structural, magnetic, and electrical studies on polycrystalline transition-metal-doped $BiFeO_3$ thin films. J. Phys. C **21**, 036001 (2009)
19. J. Liu, M.Y. Li, L. Pei, J. Wang, Z.X. Hu, X. Wang, X.Z. Zhao, Effect of Ce and Zr codoping on the multiferroic properties of $BiFeO_3$ thin films. Europhys. Lett. **89**, 57004 (2010)
20. G.L. Yuan, S.W. Or, Multiferroicity in polarized single-phase $Bi_{0.875}Sm_{0.125}FeO_3$, ceramics. J. Appl. Phys **100**, 024109 (2006)
21. R. Ramesh, N.A. Spaldin, Multiferroics: progress and prospects in thin films. Nat. Mater. **6**, 21 (2007)
22. M. Fiebig, Revival of the magnetoelectric effect. J. Phys. D **38**, R123 (2005)
23. C.-H. Yang, J. Seidel, S.Y. Kim, P.B. Rossen, P. Yu, M. Gajek, Y.H. Chu, L.W. Martin, M.B. Holcomb, P. Maksymovych, L. Scullin, R. Ramesh, Electric modulation of conduction in multiferroic Ca-doped $BiFeO_3$ films. Nature **8**, 485 (2009)
24. A.K. Vishwakarma, P. Tripathi, A. Srivastava, A.S.K. Sinha, O.N. Srivastava, Band gap engineering of Gd and Co doped BiFeO3 and their application in hydrogen production through photoelectrochemical route. Int. J. Hydrog. Energy (2017). doi:10.1016/j.ijhydene.2017.07.153
25. F. Wang, D. Chen, N. Zhang, S. Wang, L. Qin, X. Sun, Y. Huang, Oxygen vacancies induced by zirconium doping in bismuth ferrite nanoparticles for enhanced photocatalytic performance. J. Colloid Interface Sci. (2017). doi:10.1016/j.jcis.2017.08.056
26. M.A. Ahmed, S.F. Mansour, S.I. El-Dek, M.M. Karamany, Hybridization between microstructure and magnetization improvement in lead and RE co-doped $BiFeO_3$. J. Rare Earths **34**(5), 495–506 (2016)
27. H. Gao, J. Tian, H. Zheng, F. Tan, W. Zhang, Magnetic and optical properties of La-doped BiFeO3 films prepared by sol–gel route. J. Mater. Sci. **26**(2), 700–704 (2015)
28. P. Suresh, S. Srinath, Effect of La substitution on structure and magnetic properties of sol-gel prepared $BiFeO_3$. J. Appl. Phys. **113**, 17D920 (2013)
29. A.H.M. Gonzalez, A.Z. Simões, L.S. Cavalcante, Soft chemical deposition of $BiFeO_3$ thin films. Appl. Phys. Lett. **90**, 052906-1–052906-3 (2007)
30. A.Z. Simões, R.F.C. Pianno, E.C. Aguiar, J.A. Varela, E. Longo, Effect of niobium dopant on fatigue characteristics of $BiFeO_3$ thin films grown on Pt electrodes. J. Alloy. Comp. **479**, 274–279 (2009)
31. L.V. Costa, R.C. Deus, M.A. Zaghete, A. Ries, F. Moura, J.A. Varela, Experimental evidence of enhanced ferroelectricity in Ca doped $BiFeO_3$. Mater. Chem. Phys. **144**, 476–483 (2014)
32. R.A. Young, A. Sakthivel, T.S. Moss, C.O. Paiva-Santos, DBWS-9411 - an upgrade of the DBWS*.* programs for Rietveld refinement with PC and mainframe computers. J. Appl. Cryst. **28**, 366–367 (1995)
33. D.M. Rietveld, A profile refinement method for nuclear and magnetic structures. J. Appl. Cryst. **2**, 65 (1969)
34. D.L. Bish, Quantitative mineralogical analysis using the Rietveld full-pattern fitting method J.E. Post. Am. Miner. **78**, 932 (1993)
35. L. Lutterotti, S. Matthies, H.R. Henk, Material Analysis Using Diffraction: a user friendly program for Rietveld texture analysis and more. Proceeeding of the twelfth international conference and textures of materials (ICOTOM-12), vol. 1 (1999), p. 1599. http://www.ing.unitn.it/~maud/
36. L. Lutterotti, S. Matthies, H.R. Wenk, A.J. Schultz, J.J. Richardson, Texture and structure analysis of deformed limestone from neutron diffraction spectra. Appl. Phys. **81**, 594 (1997)
37. G. Will, *Powder diffraction: the Rietveld Method and the two stage method to determine and refine crystal structures from powder diffraction data* (Springer, Berlin, 2006) pp. 44–69
38. T. Barth, G. Lunde, Lattice constants of the cuprous and silver halides. Z. Phys. Chem. **121**, 78 (1926)
39. C. Lepoittevin, S. Malo, N. Barrier, N. Nguyen, G. Van Tendeloo, M. Hervieu, Long-range ordering in the $Bi_{1-x}Ae_xFeO_{3-x/2}$ perovskites: $Bi_{1/3}Sr_{2/3}FeO_{2.67}$ and $Bi_{1/2}Ca_{1/2}FeO_{2.75}$. J. Solid State Chem. **181**, 2601 (2008)
40. J. Tian, H. Gao, H. Deng, L. Sun, H. Kong, P. Yang, J. Chu, Structural, magnetic and optical properties of Ni-doped TiO_2 thin films deposited on silicon(1 0 0) substrates by sol–gel process. J. Alloys Compd. **581**, 318–323 (2013)
41. J. Zhang, Q. Xu, Z. Feng, M. Li, C. Li, Importance of the relationship between surface phases and photocatalytic activity of TiO_2. Angew. Chem. **47**(9), 1766–1769 (2008)